

## Megashears and hydrothermalism at the Martian crustal dichotomy in Valles Marineris

Joanna Gurgurewicz <sup>1</sup>, Daniel Mège <sup>1</sup>, Frédéric Schmidt <sup>2,3</sup>, Sylvain Douté<sup>4</sup> & Benoit Langlais <sup>5</sup>

Observations of ancient deep deformation systems on Mars are important for constraining planetary dynamics, as well as to identify potential mineral resources. However, such systems were thought to be unexposed and inaccessible to analysis. Here, we apply structural and hyperspectral analyses, and correlate results with magnetic anomaly patterns, to investigate two large right-lateral brittle-ductile shear zones and fault megabreccia exposed in the deepest parts of Valles Marineris. The shear zones follow the trace of the edge of the Borealis impact basin, thought to represent the planetary dichotomy boundary. We identify hydrothermally altered mafic igneous rocks in the sheared basement. We suggest that the shear system was initiated as basin ring fault system in the pre-Noachian, with further reactivation up until the Hesperian, and may still be a potential source of marsquakes. Hydrothermal circulation through the shear zones may have initiated primary mineralizations which are promising for base and rare metal exploration.

<sup>1</sup>Centrum Badań Kosmicznych Polskiej Akademii Nauk (CBK PAN), Bartycka 18A, 00-716 Warszawa, Poland. <sup>2</sup>Université Paris-Saclay, CNRS, GEOPS, 91405 Orsay, France. <sup>3</sup>Institut Universitaire de France (IUF), Paris, France. <sup>4</sup>Université Grenoble Alpes, CNRS, CNES, IPAG, 38000 Grenoble, France. <sup>5</sup>Nantes Université, Université d'Angers, Le Mans Université, CNRS, UMR 6112, Laboratoire de Planétologie et Géosciences, 44000 Nantes, France. ✉email: [jgur@cbk.waw.pl](mailto:jgur@cbk.waw.pl)

The Hesperian and Amazonian tectonics of Mars are well characterized owing to plentiful exposures. However, the pre-Noachian and Noachian rocks are obscured by extensive resurfacing in many regions. Where exposed, tectonics is seen to be locally complex<sup>1,2</sup> as expected from remote geochemistry and geophysics<sup>3</sup>. In this paper, we report on two large shear zones exposed in a deep erosional window that formed in the brittle-ductile domain of the crust early in Mars history and located in the area between the northern Valles Marineris trough system and the planetary dichotomy boundary (PDB).

The Valles Marineris trough system is exposed atop a broad topographic dome that is superimposed on the Tharsis rise<sup>4</sup>. The dome's large free-air gravity anomaly<sup>5</sup> is consistent with an upward flexural response of crust thickened between the Late Noachian and Early Hesperian. Trough nucleation<sup>6,7</sup> has been interpreted as the consequence of differential loading of the thickening Tharsis volcanic pile over the pre-existing step in basement topography that has been associated with the Borealis basin, which may have formed by an oblique impact event early in Mars history, probably around 4.5 Ga<sup>4,8,9</sup>. Extrusive volcanic activity associated with the early growth of Tharsis could have led to differential (north-south) loading of the crust across the PDB, producing a circumferential flexural uplift some 500–1000 km wide<sup>4</sup>, growth of large-scale igneous dikes<sup>6,10</sup>, dilational normal faulting<sup>11,12</sup>, and subsidence of crustal blocks parallel to them<sup>4,6,7</sup>. During the Hesperian, the troughs were partly filled by the Interior Layered Deposits (ILD), consisting of sequences of sulfate-rich layers formed by chemical evolution in an acidic environment of atmospherically-deposited ice, dust, and sulfur-rich volcanics<sup>13,14</sup>, leading to continued or renewed subsidence. The ILD were then locally eroded down by several kilometers. The reported shear zones are located in areas where ILD erosion attains ~6 km vertically. However, the exposed surface is not the surface of the Hesperian plateau. We show that it is a deeper crustal level in which complex deformation and intrusive activity is apparent, opening a window into the proto-Valles Marineris history.

## Results and discussion

### Identification of a basement unit in northern Valles Marineris.

The deepest parts of eastern Ophir and Hebes Chasmata (Fig. 1) display complex terrains that have not been characterized before. These terrains are fully covered by MRO/HiRISE images. Mapping at the HiRISE scale (Fig. 1 and Supplementary Figs. 1, 2) reveals highly deformed light-toned rocks. Most of them form a massive unit, with fracture patterns reminiscent of crystalline rocks. This rock unit also contains dikes and other intrusions. The layering of distinct colors indicates that its composition is not uniform, and suggests mechanical contrasts that may influence the deformation style. Although generally light-toned, the morphology of these rocks is distinct from that of the nearby ILD, also light-toned. Supplementary Figs. 3–7 illustrate this diversity of terrains. These terrains were not identified in earlier geologic maps of Valles Marineris, in which they were attributed to Amazonian landslide-related or other surficial processes (see Supplementary Discussion).

Nonlinear unmixing<sup>15</sup> of hyperspectral data from MRO/CRISM (see Methods section) applied to three regions of interest (ROI) where the basement rock is well exposed (see Supplementary Methods and Supplementary Data 1<sup>16</sup>) shows that the rock is mafic and contains olivine, pyroxenes, and plagioclases, associated with various sulfates (Fig. 2). It gives a primary rock composition similar to one of the bright rocks exposed in other places of Valles Marineris<sup>17</sup> and at the outer Hellas impact ring structure<sup>18</sup>. Should the retrieved primary mineral abundances from the analyzed CRISM data be representative of the exposed rock, from conventional

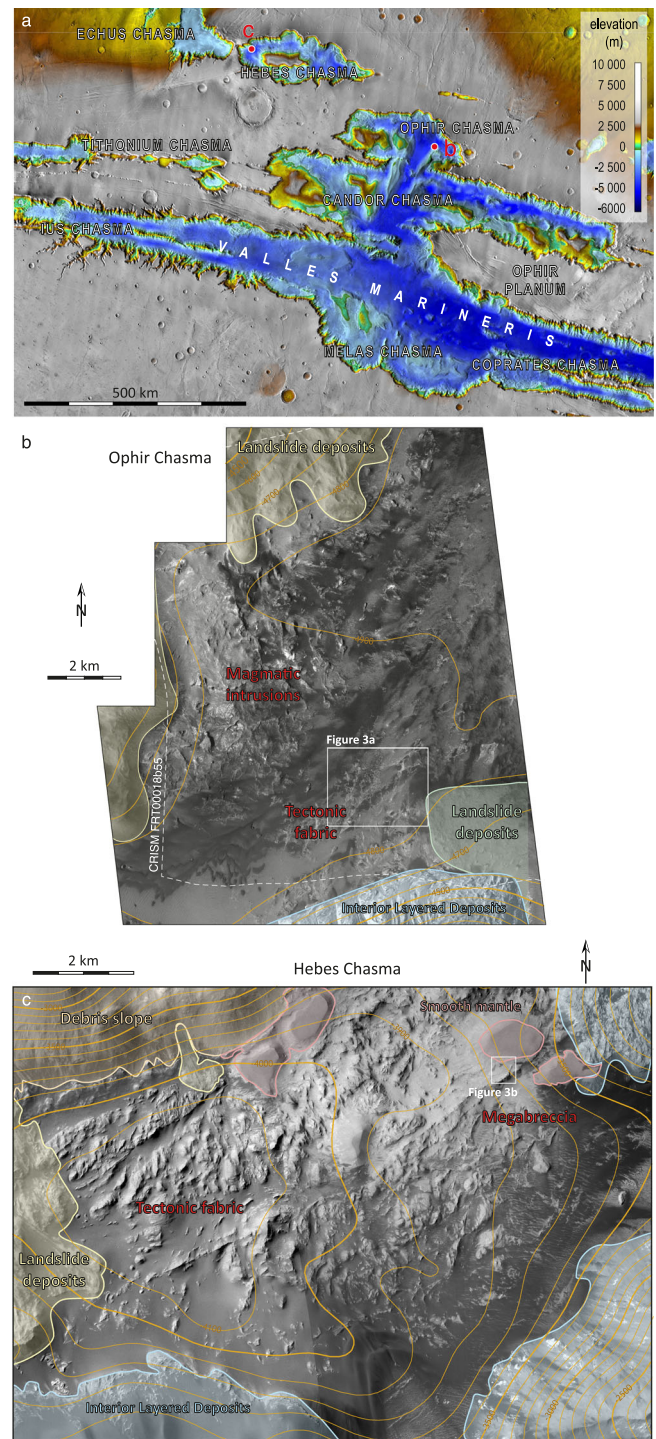


**Fig. 1** Location map and interpreted CTX mosaic<sup>91</sup> of the two study areas in Valles Marineris. **a** Location map: THEMIS Day IR Global Mosaic<sup>92</sup> merged with the 128 ppd MOLA digital terrain model<sup>93</sup>. The white dashed line indicates a continuation of the Hebes tectonic fabric as a graben system onto the plateau above the chasma. **b** Interpreted CTX mosaic<sup>91</sup> of Ophir Chasma. **c** Interpreted CTX mosaic<sup>91</sup> of Hebes Chasma. The topographic information (contours, in meters) in **(b)** and **(c)** is extracted from an HRSC topographic mosaic of Valles Marineris (credit: ESA/DLR/Freie Univ. Berlin).

igneous rock nomenclature, it would be of olivine-gabbro-norite (ROI1) or troctolite (ROI2 and ROI3) composition. In that case, the primary mineral assemblage gives a magmatic origin, with copiapite, jarosite, and szomolnokite additionally suggesting hydrothermal alteration of sulfides. A similar assemblage of sulfates found in

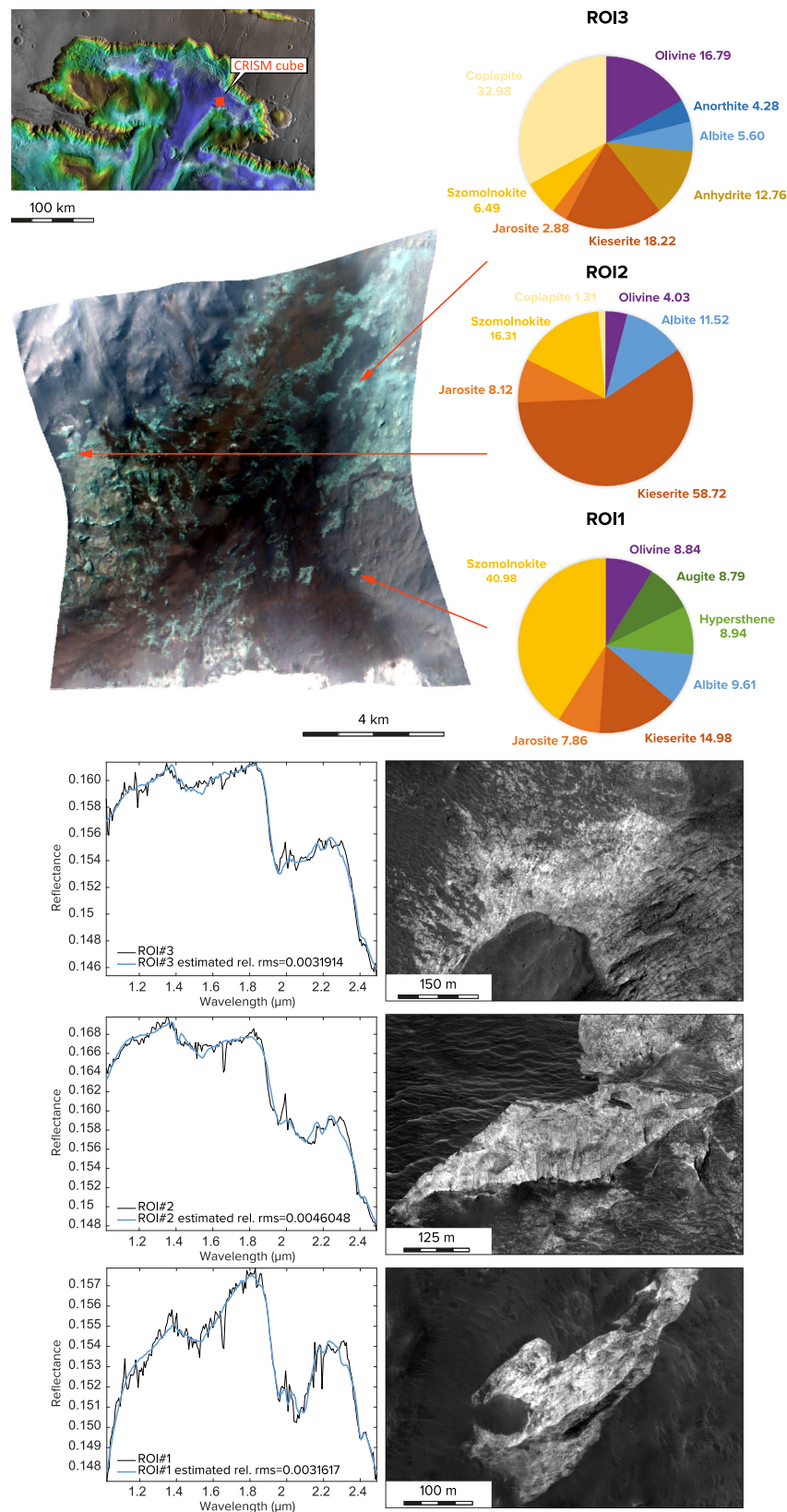


**Fig. 2 Results of nonlinear spectral unmixing applied to the three selected regions of interest (ROI).** Location of the three ROIs on CRISM image FRT00018b55 (bands R: 233, G: 78, B: 13), mineral relative abundances, the best fit plots with the relative RMS indicated, and corresponding HiRISE images of ROI1 (ESP\_051999\_1755\_RED), ROI2 (ESP\_039525\_1755\_RED), and ROI3 (ESP\_039525\_1755\_COLOR). The result of a mixture containing pure albite and anorthite (ROI3) is interpreted as a plagioclase (albite-anorthite) solid solution. The same stands for the kieserite-szomolnokite solid solution. Credits: CRISM data: NASA/Johns Hopkins University Applied Physics Laboratory; HiRISE images: NASA/JPL/the University of Arizona. The background of the location map is THEMIS Day IR Global Mosaic<sup>92</sup> merged with the 128 ppd MOLA digital terrain model<sup>93</sup>.



Noctis Labyrinthus was also interpreted as the result of hydrothermal activity<sup>19</sup>. Anhydrite, identified in veins in Gale crater<sup>20</sup> and interpreted as originating from basaltic rock weathering, could alternatively be of primary origin<sup>21</sup>, storing magmatic sulfur prior to breaking down and releasing it to the hydrothermal sulfates<sup>22</sup>. Kieserite may come from the nearby ILD<sup>23</sup>, either transported by wind, or present in some small ILD outliers on the chasma floor. The difference between the composition of ROI1 and ROI2-3 confirms that the exposed basement does not have a uniform composition; in fact, HiRISE image analysis suggests a larger diversity of rock types, as illustrated by vertical banding (Supplementary Fig. 7). Gabbronorite and troctolite composition, layering, and the presence of minerals coming from alteration of sulfides make a geological assemblage that characterizes some magmatic cumulates on Earth, e.g., at the Longwood Range in New Zealand<sup>24</sup>.

The retrieved mineralogical composition is markedly distinct from the ILD composition<sup>23</sup>. Aside from compositional information, the thickness of the dikes, tens of meters, and the presence of other intrusive bodies at the surface also indicate that the observed surface is exhumed, with probable kilometers of crust removed by erosion prior to ILD deposition, like dikes of similar thickness exposed on terrestrial continental shields<sup>7</sup>. Chasma formation was therefore driven not only by tectonic extension, but also substantial erosion, that the upper Hesperian ILD age<sup>25</sup> constraints to not later than lower Hesperian. The age of the basement rocks themselves must be older, perhaps Noachian or pre-Noachian. Both in the Ophir and Hebes Chasmata, this basement is discontinuously exposed, partly blanketed by low albedo deposits, including mottled terrain, a smooth mantle of probably airfall origin, and dune fields (Supplementary Figs. 1–3). This generally smooth material, devoid of large impact craters, explains why earlier mappers considered it to be of the Amazonian age (see Supplementary Discussion).

**Brittle-ductile shear zones and fault megabreccia in the basement unit.** We now focus on the deformation affecting the light-toned, mafic basement unit underlying the dark mantle terrains. Structural analysis (Fig. 3 and Supplementary Figs. 1, 2) reveals

S-C and S-C-C' structures that point to right-lateral kinematics, with the main shears (C) oriented N055E (Ophir) and N065E (Hebes). Their formation implies shearing in a brittle-ductile regime. In the Hebes shear zone, fractures having walls separated laterally by up to one hundred meters are observed on a HiRISE image. They contain rock fragments of longer dimensions, up to several tens of meters. HiRISE color information reveals at least two different rock compositions (greyish and yellowish). The fragments are incorporated into a bright matrix bounded by the fracture walls. We interpret them as a megabreccia that testifies to brittle deformation.

The minimum shear zone width is estimated to be ~1 km in Ophir Chasma and 3 to 3.5 km in Hebes Chasma (Fig. 1 and Supplementary Figs. 1, 2). Using scaling relationships to evaluate shear zone displacement from their measured width, and then shear zone length from displacement (see Methods section), displacements along these structures may range between a few tens to several hundreds of kilometers, implying, in turn, horizontal shear zone extents of several hundred to perhaps several thousand kilometers (Supplementary Fig. 8).

The relative timing of brittle and brittle-ductile deformation could not be determined from mapping. For instance, cross-cutting relationships between tectonic structures formed in the brittle field (e.g., megabreccia) and the ones formed in the brittle-ductile field (e.g., sigmoidal fabric), or evidence of tectonic structure reactivation, were not observed. However, none of these deformation patterns are seen to extend in the ILD nor on the plateau surrounding the troughs, indicating that they formed earlier than the Hesperian plateau surface and ILD<sup>1</sup>. The Hebes shear zone extends west and, to a lesser extent, north on the Hesperian plateau as a narrow graben system (Fig. 1a and Supplementary Fig. 9). It may suggest reactivation of the shear zone in extension over as much as ~900 km, up to Noctis Labyrinthus, after the deposition of the early Hesperian Tharsis volcanics.

The formation of brittle-ductile shear zones several kilometers below the current surface requires that the Martian crust was wet and weak, in agreement with several works (see Methods section). The available water sources may have included abundant

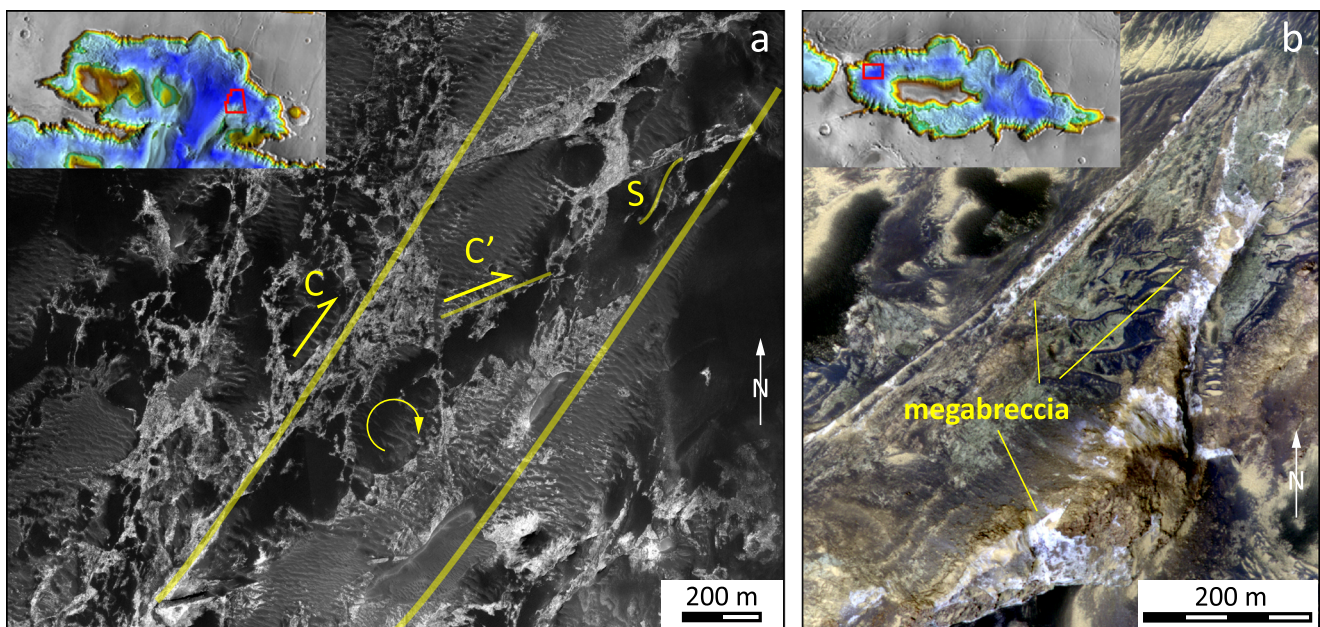


**Fig. 3 Deformation patterns in the Ophir and Hebes shear zones. a** Main exposure of the Ophir shear zone, highlighting S-C-C' structures indicative of brittle-ductile deformation (HiRISE image ESP\_017754\_1755). **b** Fault megabreccia exposed along the Hebes shear zone (HiRISE image ESP\_040211\_1790). Detailed structural mapping and context images are provided in Supplementary Figs. 1, 2. Credit: HiRISE images: NASA/JPL/the University of Arizona.



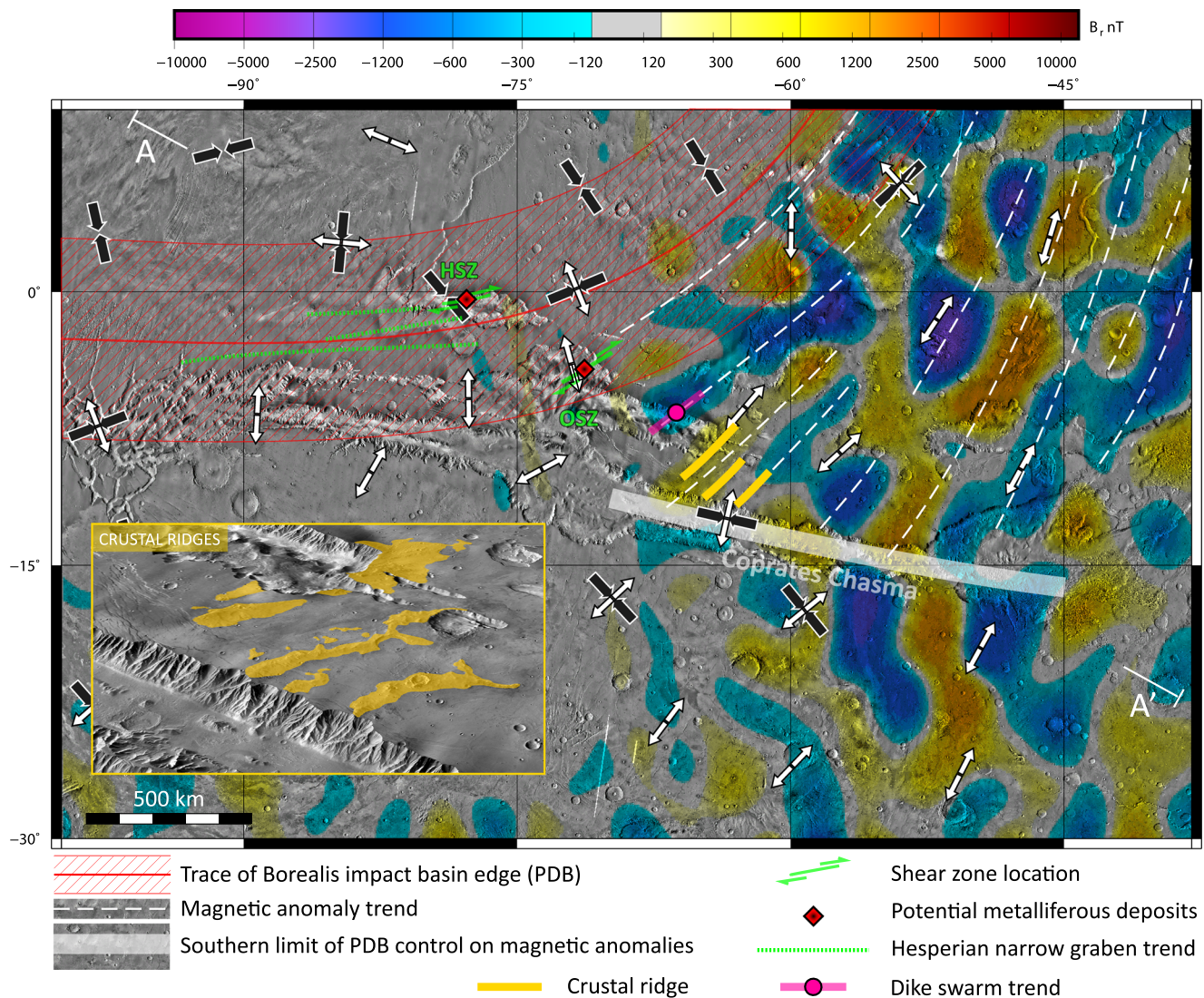


**Fig. 4 The Ophir shear zone (OSZ) and Hebes shear zone (HSZ) in the context of the Planetary Dichotomy Boundary (PDB), the radial component of the magnetic anomaly at the surface, and some other tectonic elements.** The trace of the Borealis impact basin, located with  $\pm 5^\circ$  of uncertainty, is after Andrews-Hanna<sup>4</sup>. The shear zones and narrow grabens follow the PDB, and are interpreted as reactivated PDB ring structures. The OSZ extends northeastwards between magnetic anomalies of opposite polarity. The circumferential linear magnetic lineations are interpreted as hydrothermal transformation of additional magma-intruded ring structures. Crustal ridges and a NE-trending dike swarm are parallel to magnetic anomalies. The inset shows a 3D view of the largest ridges, the pre-Noachian to early Noachian, in which they are observed in orange. Additional analysis of these ridges and dike swarm is in Supplementary Fig. 12. A–A' locates the magnetic profile shown in Supplementary Fig. 10. Arrows are simplified principal stress trajectory patterns from the thin-shell flexural model of Andrews-Hanna<sup>4</sup>; comprehensive results obtained in the study area are reproduced in Supplementary Fig. 13. White arrows indicate the tensile horizontal principal stress direction and large tensile stress magnitude. Black arrows indicate the most compressive horizontal principal stress direction and strongly negative tensile stress magnitude. Combined white and black arrows indicate weak tensile stress magnitude. The background is THEMIS Day IR Global Mosaic<sup>92</sup>; the topography is from HRSC (credit: ESA/DLR/Freie Univ. Berlin).

Noachian groundwater<sup>26</sup>, crustal serpentinization in relation to PDB formation, then deserpentinization and water release to the surrounding rocks in response to the thermal events associated with the formation of early Tharsis<sup>27</sup>, as well as juvenile water from Tharsis magmas. The heat advected by the fluids contributed to warm the surrounding crust, leading to a variable and locally steep thermal gradient during periods of active magmatism<sup>28</sup>, perhaps generating crustal strength contrasts at local scales.

**Shear zone significance.** Our findings and the constraints they yield for an understanding of the evolution of the Valles Marineris region before the chasma opening are the following: (1) The

shear zones are located near the PDB, and their trend is parallel (Hebes) or nearly parallel (Ophir) to it (Fig. 4). (2) The Hebes shear zone is associated with megabreccia in a bright matrix within thick fractures (Fig. 3c), and the Ophir shear zone basement unit includes megabreccia facies (Supplementary Figs. 4–6). (3) They are also located in the transitional area between the weakly magnetized lowlands crust in the north and the intensely magnetized highlands crust in the south, thought to mark the margin of the Borealis basin<sup>29</sup> (Fig. 4 and Supplementary Fig. 10). This transition was modified by Tharsis thermal events<sup>30</sup>, which started in the Noachian after the Martian dynamo shut down, erasing most of the magnetization in the shear zone area (Supplementary Fig. 11). (4) The trend of the shear zones and the Borealis impact edge is parallel to the orientation of elongated

crustal magnetic anomalies north of Coprates Chasma (Fig. 4). It was inferred that the impact occurred around 4.5 Ga, while the early dynamo was active<sup>31</sup>, strengthening the interpretation of a geological connection between them. (5) The westernmost radial magnetic anomalies north of Coprates Chasma are aligned with several crustal ridges of volcanic<sup>25</sup> or tectonic<sup>17</sup> origin up to 1 km high, formed in pre-Noachian to early Noachian terrain (Fig. 4). (6) Circumferential magnetic anomalies are observed around some impact craters and basins on Earth, where they result from the formation of magnetic minerals by impact-induced long-lasting hydrothermal activity<sup>32,33</sup>. (7) We note that the crustal ridges display channels restricted to the Noachian or pre-Noachian terrains, indicating water flows (Supplementary Fig. 12). The ridges also display surface fractures of similar, magnetic anomaly parallel orientation. (8) The NE-trending tectonic fabric is aligned with a NE-trending dike swarm on Candor Chasma walls (Fig. 4, Supplementary Figure 12), revealing intrusive magmatism along these magnetic anomalies. (9) Stress trajectories in the Valles Marineris region in response to PDB flexural loading by Tharsis using a thin-shell approach<sup>4</sup> are adapted to the tectonic deformation observed today. In spite of its simplicity (rock failure, friction, and long-term crustal viscous relaxation, are not taken into account), the model yields several major results. Tensile deviatoric stress is predicted to be high in the crustal portion of the Valles Marineris area between the PDB and Coprates Chasma. The tension axis is approximately parallel to the magnetic lineations (Fig. 4, with detailed analysis in Supplementary Fig. 13): the tectonic and magnetic fabrics are parallel. A major implication is that the magnetic anomaly patterns correspond to tectonic features. This inference is consistent with the observations made at the crustal ridges and the orientation of the Candor Chasma dike swarm. (10) In the Ophir and Hebes shear zone areas, the orientation of the principal stress trajectories in the flexural model<sup>4</sup> is in agreement with the observed right-lateral shear zone kinematics. The expected extensional regime is also consistent with an extension perpendicular to chasma orientation. (11) South of Coprates Chasma, the stress trajectories are no longer aligned with the magnetic anomalies, which perhaps indicates that magnetization is controlled by a crustal structure or composition distinct from those prevailing north of Coprates Chasma.

These elements suggest a model of crustal evolution in Valles Marineris until the opening of the main chasmata (Fig. 5). It explains not only the formation and kinematics of the shear zones, but also a series of geological features, the formation of which has remained elusive. They include the crustal ridges, the chasma-perpendicular dike swarm in Candor Chasma, the peculiar orientation of some narrow grabens between Syria Planum and Hebes Chasma, and the linear nature of magnetic anomalies north of Coprates Chasma.

The relationships between the shear zone, PDB, and anomalies are explained here by basin tectonics<sup>34</sup> applied to the Borealis basin. Formation of the Borealis basin at ~4.5 Ga generated circumferential normal faults filled with megabreccia, and crustal warming propagated from the molten crust in the impact area<sup>9</sup>. Hydrothermal circulation started along the fault pathways (Fig. 5a), mobilizing the water present in the crust, and perhaps also from the impactor. The megabreccia in the Ophir Chasma basement unit may have formed at that time, too, as an impact megabreccia, like the one interpreted around the Hellas basin<sup>18</sup>, as well as the Candor Chasma dike swarm as an impact-related ring dike system.

The duration of hydrothermal activity was shorter than the duration of the dynamo (Fig. 5b). It is poorly constrained, but for a Hellas size impact basin, it was estimated to be in the order of 10 My<sup>35</sup>. Uncertainty arises from parameters such as post-impact

crustal permeability and water abundance, as well as from the difficulty of modeling fine-scale processes in response to such a large-scale event. The four times larger Borealis basin size, based on gravity and topography<sup>8</sup>, may have much lengthened the duration of hydrothermal activity. The dynamo activity lasted until 4.1 Ga or even later in the late Noachian<sup>31</sup>, leaving at least 400 My for the hydrothermal activity to gradually stop and record the succession of polarity inversions while cooling to the Curie temperature.

The location and orientation of the Ophir and Hebes shear zones suggest that they may have been segments of ring normal faults. Similar to the other impact basins, many other ring faults should have fractured the crust in response to the impact. The observed elongated magnetic anomalies of alternating polarity may underline these structures. The hydrothermal minerals detected in the basement of the Ophir Chasma shear zone would therefore be the exposed equivalent to currently buried hydrothermal minerals that generated the observed magnetic anomalies.

In the late Noachian, adjustment of the Borealis basin load should have been achieved, through reactivation of the basin faults, decreasing the topographic difference between the highlands and lowlands (Fig. 5c). The geologic context of the Ophir and Hebes chasmata dramatically changed under the combined influence of the growth of the Tharsis load<sup>36</sup> and the major PDB crustal discontinuity. The flexural loading model of Tharsis over the PDB<sup>4</sup> predicts strike-slip reactivation along the basin ring structures in the Ophir and Hebes chasmata, resulting in the observed shear zones (Fig. 4).

The distinct tectonic domain south of Coprates Chasma is coherent with its interpretation as the northern limit of a major Hesperian and Noachian deformation system on the Thaumasia plateau and the Coprates rise<sup>37</sup>. These early Tharsis events may have deformed the crustal magnetic fabric, which would not reflect the orientation of the Borealis basin rim anymore.

The lower Hesperian marks the beginning of flood volcanism in the Tharsis region, specifically centered at Syria Planum<sup>6,25</sup>. The lava flows loaded the crust in the Valles Marineris region prior to the opening of the chasmata (Fig. 5d), with the consequence of increasing the vertical principal stress. Chasma opening by crustal extension may simply result from the permutation between the largest and intermediate principal stresses due to crustal loading by the lavas (Fig. 5d–f). Flood lava emplacement occurred via an intrusive system including a huge dike swarm<sup>6</sup> of mafic composition<sup>38</sup>, partly cancelling crustal magnetization. New magnetization could have occurred upon dike cooling in response to the external or to the nearby crustal magnetic field. However, the external field is not stable and unlikely to produce consistent patterns all over the dikes. A new magnetization related to nearby magnetization would be much less intense than the original one and is unlikely to be detected from orbit.

The shear zones identified in the Ophir and Hebes chasmata can therefore be understood in a scenario in which an inherited crustal fabric is reactivated (Fig. 5f, stage 1), additional crustal loading increases the differential stress (stage 2), ending up with nucleation of the main chasma faults in tension (stage 3). The edge of the Borealis basin west of Hebes Chasma is nearly parallel to the Valles Marineris chasmata, which explains why the Hebes shear zone was there reactivated in tension, forming some narrow grabens.

It is apparent from this geological context that the hydrothermal activity identified in the Ophir and Hebes shear zone basement may have been widespread. Coprates Chasma, as a major tectonic and magnetic boundary, may represent the southern end of this hydrothermal system in the highlands crust.



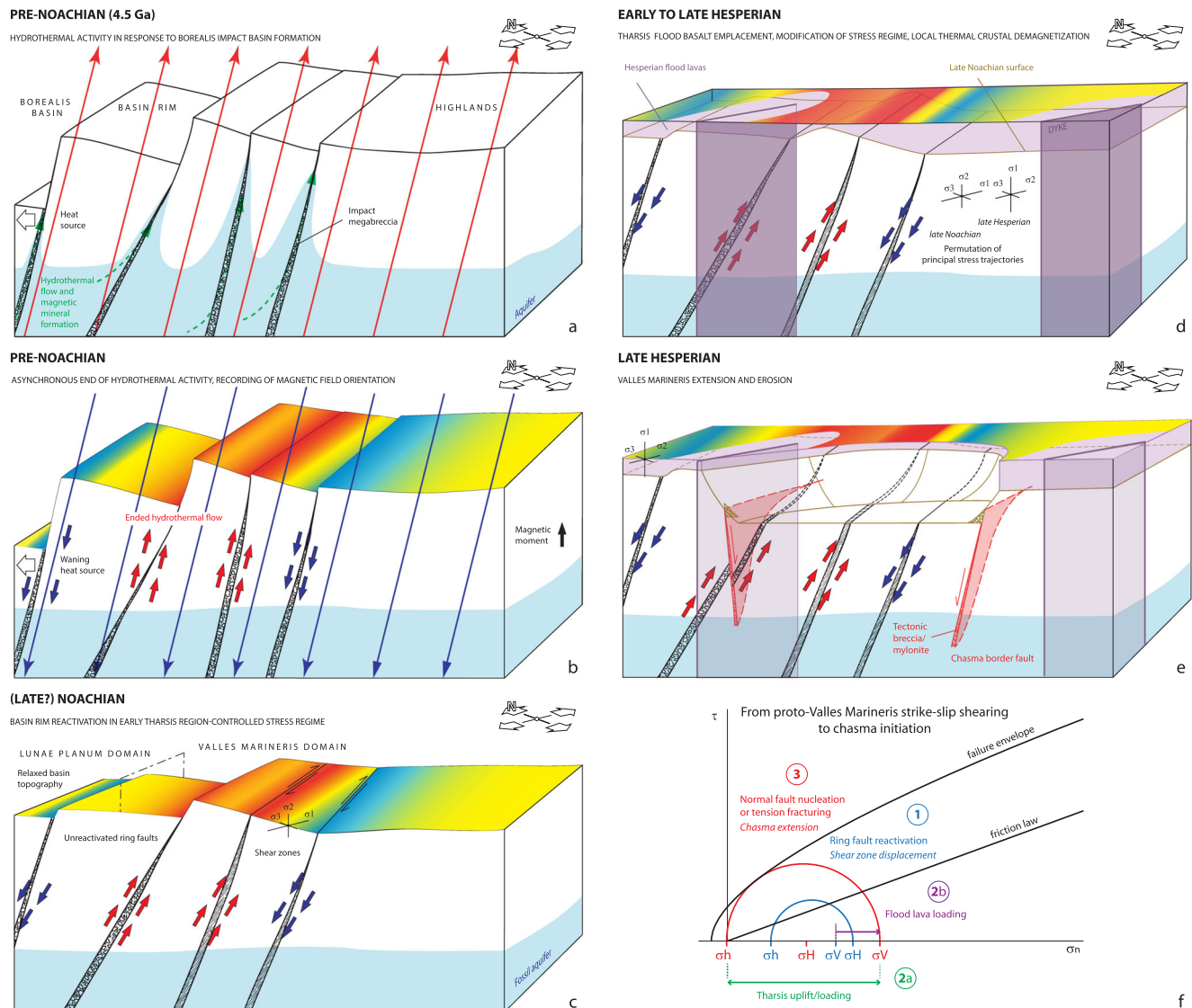


**Fig. 5 Proposed scenario of the evolution of the Valles Marineris crust. a–e** Crustal evolution stages. **f** Pre-Noachian to Hesperian evolution of stress state and brittle deformation of the Valles Marineris crust in response to Tharsis thermal events.

Evidence of hydrothermal activity at the PDB in the Valles Marineris region suggests that the weak, 10 km thick crustal layer found at the InSight landing site<sup>39</sup>, also located at the PDB area, might be a similarly altered mafic basement rock.

Brittle-ductile shear zones are one of the contexts where metalliferous mineralizations can be abundant. Our results show that the Ophir and Hebes shear zones are of exceptional, if not unique, interest to search for such mineralizations. Mesothermal gold deposits on Earth (30% of mined gold) are observed in secondary structures of exhumed brittle-ductile shear zones and their shallow extension to the surface<sup>40</sup>. Au is drained in terrestrial shear zones by hydrothermal fluids, and after a complex path, concentrates in cataclastic quartz veins<sup>41</sup>. The mineralogically expressed Au is associated with As–paragenesis of Sb, W, Bi, Mo, and Pb, and in the quartz veins, with Pb, Ag, and Cu.

Assuming that the primary minerals identified using CRISM reflect the full basement rock composition, the shear zones could be sites to prospect for Ti–V oxides, which are found in terrestrial gabbro–norite–troctolite layered intrusions<sup>42</sup>. At different depth levels, stratabound Ni–Cu sulfides and chromite may have settled<sup>43</sup>, as well as platinum-group minerals, especially including

Pt, Pd, and Au<sup>24</sup>. Although the deep source of metals accumulating in the planetary crust is loosely constrained, the sheared, fluid-charged Noachian and pre-Noachian basement rocks, as well as the neighboring intrusions, may be the most favorable environments to discover such deposits.

The influence of the Borealis basin on the tectonics and hydrothermal activity in the Valles Marineris region, and the implications for mineralizations, open a wealth of new questions of global planetary interest. Did the crustal fabric imposed by the impact influence the evolution of the Tharsis crust in other areas? Did it play a role in the genesis of the large fracture zone that guided the NE–SW orientation of many volcanic edifices that formed on the Tharsis dome? At the opposite, the Tharsis-generated stress field was shown to control the stress system of the whole planet<sup>44</sup>. Did it reactivate other PDB-related structures? Are there other sites where PDB-related hydrothermal activity can be found? Can it be identified elsewhere, without the exceptional exposure conditions in Valles Marineris? The obliquity of the Borealis basin impactor<sup>9</sup> should have generated a crustal fracturing asymmetry<sup>45</sup>, did it affect the distribution of basin-generated mineralizations? Hydrothermal minerals were detected in the Nili Fossae and Nilosyrtris highlands<sup>46</sup>, next to the

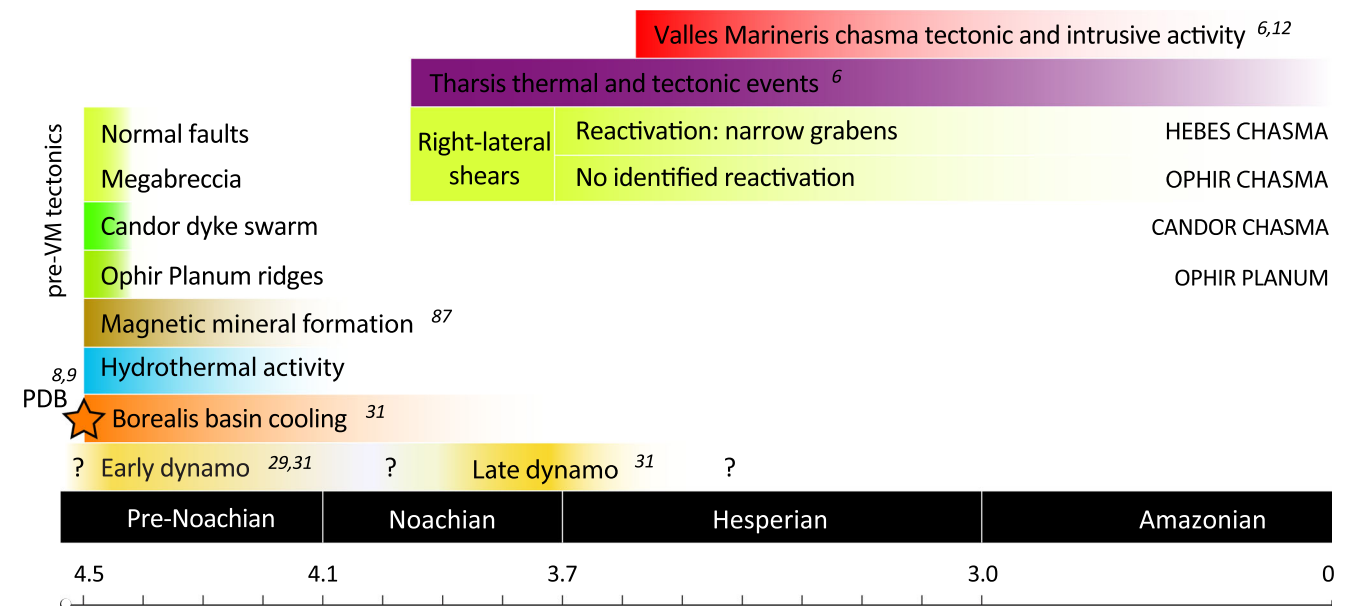


**Fig. 6 Chronology of geodynamic and tectonic events in the Valles Marineris region.** Large-scale post-Noachian tectonic activity at the shear zones is mainly restricted to the formation of narrow grabens, but as major crustal discontinuities, shear zone structures may have been occasionally active seismically until now. Numbers refer to the cited references.

PDB, which also display breccia ridges<sup>47</sup>. Do these features testify to PDB-related geologic events as well? Were the reactivated basin-related radial faults around the Hellas and Isidis basins<sup>48</sup> also prone to similar mineralizations? Finally, was the duration of hydrothermal activity associated with the Borealis basin long enough to stabilize the environmental conditions and favor the emergence of life? Radiogenic heating might have contributed to maintain a high geothermal gradient for some time<sup>49</sup>, making the northern Valles Marineris a preferential region to investigate early life in situ.

Conclusions

Our results show that the influence of the Borealis impact on the later evolution of Mars may have been underestimated (Fig. 6). Large-scale shearing of the pre-Valles Marineris basement rock testifies to major crustal deformation unrecognized before that shall be taken into account in deciphering the early Mars’ evolution. From a stress field point of view, this event is consistent with, and prefigures Valles Marineris opening, but does not prefigure the current Valles Marineris geometry. The shears probably initiated as normal faults at the time of the Borealis basin impact, as soon as ~4.5 Ga, the estimated age of the basin, while the early Martian dynamo was active<sup>31</sup>. This very long tectonic activity, combined with deep exhumation, the mafic composition of the sheared basement, and hydrothermal circulation, provide one of the most promising environments for lode deposition and concentration of metals, perhaps of cut-off grade. The idea that deep faults such as from impact basins were the locus of hydrothermal activity and played a role in crustal magnetization<sup>35,50</sup> is also validated by our analysis. The recognition of early fluid-assisted deformation and identification of alteration products associated with early hydrothermal systems suggest that at least some fundamental Martian faults may have been rheologically weak, and, therefore, susceptible to reactivation and seismic activity, from early Noachian time and perhaps into the present in the current stress field, controlled by the Tharsis load<sup>44</sup>. If still reactivated nowadays, InSight should be able to detect it in a quiet seismic environment. The marsquake of

August 25, 2021, measured by InSight in Valles Marineris, of body wave magnitude 4.1–4.2<sup>51</sup>, is consistent with such a reactivation as much as the recognized deep chasma border faults<sup>11,12,52</sup>. The deep Valles Marineris troughs should be considered a high-priority target for innovative future exploration missions. It would enable a better understanding of the early Martian dynamics, as well as offer the grounds for in situ identification of rare resources.

Methods

**Geologic mapping.** Geologic analysis was fully conducted at the HiRISE scale (25 m pixel-1) in Ophir Chasma. In Hebes Chasma, only ~75% of the shear zone area is covered with HiRISE images. Gaps were filled with CTX images (6 m pixel-1). Conventional geologic mapping was conducted with an emphasis on structural analysis. Kinematic analysis of S-C fabric is from e.g., Platt and Vissers<sup>53</sup>, following the nomenclature established by ref. <sup>54</sup>, and as modeled by ref. <sup>55</sup>. Kinematic analysis of S-C-C’ fabric is after ref. <sup>56</sup>, who also provide a review of works on this fabric.

Generation of HiRISE DTM using photogrammetry and photoclinometry.

Photoclinometry (or Shape-from-Shading, SfS) refers to the process of inferring 3D surface slopes from the intensity variations of a single shaded image. When combined with photogrammetry, as in ref. <sup>57</sup>, SfS can be used to resolve 3D details from a given shaded image and merge it with the coarse 3D information inherited from an initial DEM. In this work, we apply the HDEM method<sup>57,58</sup> to HiRISE images (1 m pixel-1) based on HiRISE stereo-derived DEMs (3 m pixel-1), and with a coarse-to-fine strategy, to further refine the DEM results (1 m pixel-1). HDEM SfS takes a single image and a co-registered coarse DEM as inputs, and iteratively refines the coarse input DEM via the minimization of a total cost function. The total cost function comprises three terms. First, the image irradiance term expresses the goodness of fit between the observed image versus its modeling from surface slopes. This modeling combines a surface atmospheric radiative transfer scheme and a realistic spatially varying bidirectional reflectance distribution function. Second, we have the integrability constraint regularization term that connects slopes to the terrain height field. Third, the photogrammetry constraint regularization term ensures the inheritance of large scales from the initial photogrammetrically generated DEM in the refined version. In this work, the spatial BRDF model results from the linear mixing of two endmember terrains, mafic, and sulfate-rich, which spectrophotometric properties are extracted from a near-coincident CRISM multi-angular acquisition sequence (FRT, HRL, HRS, EPF) using the MARS-Reco method<sup>59</sup>. The HDEM numerical scheme is repeatedly executed until a pre-set maximum number of iterations is reached or until the total cost function for the image irradiance equation, integrability constraint, and photogrammetry constraint converges.



**Determination of basement mineralogy.** We analyzed each ROI with the LinMin algorithm<sup>15</sup>, based on Primal-Dual Interior-Point Optimization<sup>60</sup>. This method assumes a linear mixture with positivity and sum-lower-than-one constraints:

$$Y \sim A \cdot S \text{ with } 0 < A < 1 \text{ and } 0 < \Sigma A < 1 \quad (1)$$

with  $Y$ , the ROI spectra,  $A$  the abundance (that are estimated), and  $S$  the end-member spectra (assumed to be known). The spectra  $S$  are from spectral libraries and have been measured in laboratory conditions, as described in Supplementary Methods. We also included flat and slope spectra, as described in ref. <sup>15</sup>, to reduce the effect of aerosols and discrepancies between laboratory and remote sensing conditions (grain size, geometry, aerosols in the atmosphere).

In order to improve the fit, we also introduce a nonlinear unmixing based on the fact that grain size changes can be simply modeled by  $S \cdot e^C + C$ , with  $e$  an exponent factor, specific to each spectrum, and  $C$  a constant value. This new model can be formulated as:

$$Y \sim A \cdot S \cdot e^C \text{ with } 0 < A < 1 \text{ and } 0 < \Sigma A < 1 \quad (2)$$

We solved this problem using the Nelder-Mead Simplex Method<sup>61</sup> to estimate the optimum  $e$ , including the LinMin algorithm<sup>15</sup>, by minimizing the reconstruction RMS. Unfortunately, this nonlinear procedure is much more computationally expensive than LinMin and not possible on a full CRISM cube. Nevertheless, for the ROI spectra selected for this work, this method is perfectly fitted. One has to note that retrieved abundances may differ from actual mineral abundance in the rock. Nevertheless, from the extensive experiments conducted, the detection of minerals from observed spectral features is robust. There is thus high confidence in the mineral assemblage for all ROIs.

A detailed description of the mineralogical analysis leading to the results presented in Fig. 2 is provided in Supplementary Methods. A synthesis of the mineral detections from spectral unmixing experiments is given in Supplementary Table 6. The spectral unmixing outputs are provided in Supplementary Data 1<sup>16</sup> as plots and ASCII files.

**Displacement scaling.** Displacement scaling relates the width ( $w$ ) or length ( $L$ ) of tectonic structures (such as faults and shear zones) against their maximum displacement ( $D$ ), along the whole range of rheological conditions in the crust. It is used as one of the tools to constrain the mechanical properties of the fractures and their host rock<sup>62–65</sup>. A broad agreement has been found over the years that for most tectonic structures, both ( $w$ ) and ( $L$ ) linearly scale with ( $D$ ), irrespective of rock composition. However, from measurements reported in the literature, the possibility exists that for shear zones,  $D/L$  follows a power law, with an exponent of 1.5<sup>65,66</sup>. In displacement scaling, the size of datasets available in the literature is not large enough to infer statistics, and  $D/w$  and  $D/L$  scaling cannot be used to predict one of the three parameters from the others accurately. Here we use  $D/w$  and  $D/L$  plots to evaluate the order of magnitude of displacement at the Ophir and Hebes shear zones from the minimum measured width, inferred from the exposures, then to evaluate the order of magnitude of shear zone length, from the displacement.

In the first step, the width of the Ophir and Hebes shear zones are measured using the spacing major shears that bound the zone of most intense deformation on HiRISE images (see Supplementary Figs. 1 for the Ophir shear zone and 2 for the Hebes shear zone). In Ophir Chasma, the width of the exposed shear zone is 1 km. In Hebes Chasma, the width is between 3 (“Hebes1” in Supplementary Fig. 8) and 3.5 km (“Hebes2”).  $D/w$  scaling is done based on a dataset of shear zones of similar dimensions<sup>60</sup>. We calculate the average  $D/w$  value for this dataset: 63, and assume that the same value applies to the Ophir and Hebes shear zones. One order of magnitude is added as a vertical error bar.

In the second step, this ( $D$ ) range is used to evaluate the length of the shear zones. Three datasets for shear zones are available in the literature<sup>62,66</sup>, among which a continental shear zone dataset is for shear zones of dimensions comparable to the Ophir and Hebes shear zones, which we use in this work<sup>67</sup>. We consider both linear (Supplementary Fig. 8b) and power law scaling with an exponent of 1.5<sup>66,67</sup> (Supplementary Fig. 8c). The average  $D/L$  for the continental shear zone dataset is 0.172. Assuming a linear relation between ( $D$ ) and ( $L$ ), the scaling line  $D = 0.172 L$  is used as a proxy for the Martian shear zones. Using the ( $D$ ) range calculated earlier, a ( $L$ ) range is calculated for the Ophir shear zone by projecting the ( $D$ ) range along the scaling line. Two ( $L$ ) ranges are calculated for the Hebes shear zone, corresponding to the 3 and 3.5 km measured widths. A horizontal error of one order of magnitude is attributed to the ( $L$ ) ranges. As a second option, it is assumed that the continental shear zone dataset follows the power law of exponent 1.5. The ( $D$ ) ranges are then projected onto this scaling line, and similarly, a horizontal bar of one order of magnitude is applied to the corresponding ( $L$ ) range.

**Determination of potential causes for brittle-ductile crustal deformation at shallow depth in Ophir and Hebes Chasmata.** Although we know that wet rheology is more likely for Mars<sup>68</sup>, we test it first with dry mafic (diabase) rheology. Assuming that deformation occurred at a depth equal to the current chasma floor depth, ~8500 m below the closest plateaus after MGS/MOLA data, the geothermal gradient required to generate brittle-ductile deformation would be 59–65 °C km<sup>-1</sup>, assuming brittle-ductile behavior at the failure/creep transition temperature of 500–550 °C, depending on plagioclase abundance<sup>69</sup>. Another composition, such as

olivine, or diorite<sup>70</sup> would only marginally change the conclusions. A quartz rheology<sup>71</sup> would make the brittle-ductile behavior even easier to reach, but is not considered here because of the mineralogical information provided by the CRISM data processing (Fig. 2).

Since the Hesperian lava pile covering the Valles Marineris plateau did not exist when the shear zones developed, and part of the floor depth was attained by tectonic stretching, the floor might have been much closer to the topographic surface, perhaps decreasing the required depth by two. This factor is considered as a maximum, because the Noachian pile is exposed at the plateau level at the same elevation as the Hesperian lava pile 430 km away from the Ophir shear zone, at the eastern edge of Candor Chasma<sup>25</sup>, with no major change of stratigraphic levels reported along the chasma walls between eastern Candor Chasma and eastern Ophir Chasma. Increasing the required geothermal gradient accordingly yields 120 °C km<sup>-1</sup>. This value is 5–10 times the average gradient calculated in the Martian highlands during Noachian<sup>72–75</sup> and for the Hesperian extensional deformation observed around Tharsis<sup>76</sup>, and four times the gradient found during Noachian rifting south of Valles Marineris, at Thaumasia Planum, up to 33 °C km<sup>-1</sup><sup>77</sup>. However, it was suggested recently that radiogenic heating<sup>78</sup> may also have participated in substantially increasing the thermal gradient during the Noachian<sup>49</sup>.

The temperatures of 500–550 °C required to make diabase flow may actually not be needed, implying that very high thermal gradients may not be required. There is multiple evidence that crustal strength on terrestrial continents does not exceed ~50 MPa, with ductile creep occurring already at 6 km depth<sup>79</sup>. Equivalently, viscous relaxation of impact basins indicates a weak lower crust, with moderate heat flow<sup>80</sup>. Assuming a mean terrestrial crustal density of 2.7 g cm<sup>-3</sup>, the corresponding lithostatic pressure would normally be 158 MPa, implying stress reduction by a factor of 3 to 4. On Mars, assuming a basaltic crust of density of 2.9 g cm<sup>-3</sup>, 50 MPa would be located at 4.7 km depth, and if reduced by 3–4, ductile creep would occur as shallow as 1.2–1.6 km below the surface.

The first reason for such a strength decrease is the presence of free water in the crust<sup>71</sup>, which may be testified to by the CRISM detections of hydrated hydrothermal sulfates (szomolnokite and copiapite have respectively 1, and 20 molecules of water in their structure, and jarosite has three hydroxyl groups). The weakening effect of water is major whatever the creep regime, dislocation, or diffusion<sup>81</sup>. Even less than 0.1% of water<sup>79</sup> may decrease rock strength by a factor of 2 to 3<sup>69</sup>. Wet diabase<sup>82,83</sup> is therefore much weaker than dry diabase<sup>69</sup>, but perhaps more importantly, the hydrothermal paths not only locally dramatically increase heat flow, but also their pervasive penetration in the crust has a substantial warming effect that adds to the background heat flow<sup>84</sup>.

Water may originate from infiltration through Noachian runoff channels<sup>85</sup> as well as volcanic outgassing<sup>86</sup>. The water of metamorphic origin may also weaken the crust; in particular, the correspondence between the edge of the crust showing magnetic anomalies<sup>29</sup> and the geometry of the exposed shear zones (Fig. 4) suggests a genetic link. One of the explanations for crustal magnetization is serpentinization during the Noachian<sup>27,87</sup>. Serpentinization may have weakened the shear zone area in three possible ways. First, during the magnetization itself, mobilizing free water, and incorporating it into mafic minerals transformed to chrysotile<sup>27,87</sup>, reducing crustal strength<sup>88</sup> and shifting the portion of the crust exposed in the shear zone areas from the brittle toward the ductile domain. Weakening may proceed to such a point that locally serpentinite may rise through fractures by diapirism<sup>89</sup>, providing a potential explanation for intrusions mapped on Supplementary Figs. 1, 2, as an alternative to magmatic intrusions. In that case, the whole magnetized crust being serpentinized, the weak rheology of the shear zone is not an exception, the observation of brittle-ductile structures at this depth is made possible by the denudation of Valles Marineris in the eastern Ophir and western Hebes Chasmata. Secondly, shear zone area weakening may have occurred during the process of crustal serpentinization because the troughs are located near the edge of the Borealis basin, a crustal zone of density contrast where intense fluid circulation is expected to have occurred. The rheology of the shear zones in Valles Marineris would be another tectonic consequence of crustal magnetization. Thirdly, if the shear zones formed later than the crustal magnetization event, crustal weakening could have corresponded to crustal deserpentinization. For instance, under the effect of magmatic heat release at the earliest stages of the Tharsis-Syria Planum magmatic events by the end of Noachian or earliest Hesperian<sup>6</sup>, water from chrysotile structure could have been releasing west of eastern Ophir Chasma. It is also possible that partial deserpentinization occurred owing to crustal heating from below, which would explain magnetization depth as shallow as 5–10 km<sup>90</sup>. Whatever the case, the magnetization of the Martian crust by serpentinization, or deserpentinization, is likely to have involved a substantial amount of water, up to 1 km of global equivalent layer<sup>27</sup>, which should have contributed to weakening the rheology in the shear zone areas.

Finally, crustal rheology strongly depends on the strain rate; taking the viscous component of the Martian lithosphere rheology into account would decrease lithospheric strength and shallow the brittle-ductile transition depth<sup>79</sup>.

In summary, a simple dry crustal rheology cannot explain the observation of brittle-ductile deformation in the Ophir and Hebes shear zones. Several mechanisms have been identified which may explain the formation of brittle-ductile structures at the observed paleo-depth. Crustal hydration is one, and it was noted that in addition to the dramatic and well-known effect of a very small quantity of free water on the rheology of the crust, for which there is evidence in

the Noachian, hydrothermal circulation may have multiplied the geothermal gradients by several times at the scale of the exposed shear zone outcrops, a few tens of km<sup>2</sup> in size. Structural water related to crustal serpentinization or deserpentinization (or other metamorphic reactions) may provide another source of rheological weakening, perhaps in connection with the initiation of the Tharsis-Syria Planum magmatism. All these processes are not exclusive, instead, they may have been added and combined, resulting in brittle-ductile deformation in Ophir and Hebes Chasmata.

### Data availability

The HiRISE, CTX, CRISM, THEMIS, MOC, and Viking data were available from the NASA Planetary Data System at <https://doi.org/10.17189/1520303>, <https://doi.org/10.17189/1520266>, <https://doi.org/10.17189/1519573>, <https://doi.org/10.17189/1520386>, <https://doi.org/10.17189/1520255>, and <https://doi.org/10.17189/1520333>, respectively.

The HRSC digital terrain models are available from the ESA Planetary Science Archive (<https://doi.org/10.1016/j.pss.2017.07.013>).

The Supplementary Data 1 dataset is available in the following public repository: <https://gitlab.dsi.universite-paris-saclay.fr/frederic.schmidt/linearunmixing/-/tree/main/results>.

### Code availability

The CRISM data processing code is available in the following public repository: <https://gitlab.dsi.universite-paris-saclay.fr/frederic.schmidt/linearunmixing>.

Received: 10 January 2022; Accepted: 1 November 2022;

Published online: 17 November 2022

### References

- Scott, D. H. & Tanaka, K. L. Map showing lava flows in the southeast part of the Amazonis Quadrangle of Mars. U.S. Geological Survey IMAF 1280, scale 1:2,000,000. <https://doi.org/10.3133/i1280> (1981).
- Tanaka, K. L. & Davis, P. A. Tectonic history of the Syria Planum province of Mars. *J. Geophys. Res. Solid Earth* **93**, 14893–14917 (1988).
- Bouley, S. et al. A thick crustal block revealed by reconstructions of early Mars highlands. *Nat. Geosci.* **13**, 105–109 (2020).
- Andrews-Hanna, J. C. The formation of Valles Marineris: 2. Stress focusing along the buried dichotomy boundary. *J. Geophys. Res. Planets* **117**, E03006 (2012).
- Genova, A. et al. Seasonal and static gravity field of Mars from MGS, Mars Odyssey and MRO radio science. *Icarus* **272**, 228–245 (2016).
- Mège, D. & Masson, P. A plume tectonics model for the Tharsis province, Mars. *Planet. Space Sci.* **44**, 1499–1546 (1996).
- Ernst, R. E., Grosfils, E. B. & Mège, D. Giant dyke swarms on Earth, Venus and Mars. *Ann. Rev. Earth Planet. Sci.* **29**, 489–534 (2001).
- Andrews-Hanna, J. C., Zuber, M. T. & Banerdt, W. B. The Borealis basin and the origin of the martian crustal dichotomy. *Nature* **453**, 1212–1215 (2008).
- Marinova, M. M., Aharonson, O. & Apsphaug, E. Mega-impact formation of the Mars hemispheric dichotomy. *Nature* **453**, 1216–1219 (2008).
- Mège, D., Cook, A. C., Garel, E., Lagabrielle, Y. & Cormier, M.-H. Volcanic rifting at Martian grabens. *J. Geophys. Res. Planets* **108**, 5044 (2003).
- Schultz, R. A. Gradients in extension and strain at Valles Marineris, Mars. *Planet. Space Sci.* **43**, 1561–1566 (1995).
- Mège, D. & Masson, P. Amounts of crustal stretching in Valles Marineris, Mars. *Planet. Space Sci.* **44**, 749–781 (1996).
- Kite, E. S. et al. Evolution of major sedimentary mounds on Mars: Buildup via anticompensational stacking modulated by climate change. *J. Geophys. Res. Planets* **121**, 2282–2324 (2016).
- Michalski, J. & Niles, P. Atmospheric origin of Martian interior layered deposits: links to climate change and the global sulfur cycle. *Geology* **40**, 419–422 (2012).
- Schmidt, F. & Legendre, M. & Le Mouélis, S. Minerals detection for hyperspectral images using adapted linear unmixing: LinMin. *Icarus* **237**, 61–74 (2014).
- Gurgurewicz, J., Mège, D., Schmidt, F., Douté, S. & Langlais, B. Supplementary Data 1. <https://gitlab.dsi.universite-paris-saclay.fr/frederic.schmidt/linearunmixing/-/tree/main/results> (2022).
- Viviano-Beck, C. E., Murchie, S. L., Beck, A. W. & Dohm, J. M. Compositional and structural constraints on the geologic history of eastern Tharsis Rise, Mars. *Icarus* **284**, 43–58 (2017).
- Rogers, A. D. & Nazarian, A. H. Evidence for Noachian flood volcanism in Noachis Terra, Mars, and the possible role of Hellas impact basin tectonics. *J. Geophys. Res. Planets* **118**, 1094–1113 (2013).
- Thollot, P. et al. Most Mars minerals in a nutshell: various alteration phases formed in a single environment in Noctis Labyrinthus. *J. Geophys. Res. Planets* **117**, E00J06 (2012).
- Rapin, W. et al. An interval of high salinity in ancient Gale crater lake on Mars. *Nat. Geosci.* **12**, 889–895 (2019).
- Chambefort, I., Dilles, J. H. & Kent, A. J. R. Anhydrite-bearing andesite and dacite as a source for sulfur in magmatic-hydrothermal mineral deposits. *Geology* **36**, 719–722 (2008).
- Hutchinson, M. C. & Dilles, J. H. Evidence for magmatic anhydrite in porphyry copper intrusions. *Econ. Geol.* **114**, 143–152 (2019).
- Roach, L. H. et al. Testing evidence of recent hydration state change in sulfates on Mars. *J. Geophys. Res. Planets* **114**, E00D02 (2009).
- Ashley, P., Craw, D., MacKenzie, D., Rombouts, M. & Reay, A. Mafic and ultramafic rocks, and platinum mineralisation potential, in the Longwood Range, Southland, New Zealand. *N. Z. J. Geol. Geophys.* **55**, 3–19 (2012).
- Witbeck, N. E., Tanaka, K. L. & Scott, D. H. Geologic map of the Valles Marineris region, Mars. U.S. Geological Survey Geologic Investigations Series, Map I–2010, scale 1:2,000,000. <https://doi.org/10.3133/i2010> (1991).
- Palumbo, A. M. & Head, J. W. Oceans on Mars: the possibility of a Noachian groundwater-fed ocean in a sub-freezing martian climate. *Icarus* **331**, 209–225 (2019).
- Chassefière, E., Langlais, B., Quesnel, Y. & Leblanc, F. The fate of early Mars' lost water: The role of serpentinization. *J. Geophys. Res. Planets* **118**, 1123–1134 (2013).
- Eppelbaum, L., Modelevsky, M. Jr & Pilchin, A. Geothermal investigations in the Dead Sea rift zone, Israel: implications for petroleum geology. *J. Pet. Geol.* **19**, 425–444 (1996).
- Langlais, B., Thébaud, E., Houliez, A., Purucker, M. E. & Lillis, R. J. A new model of the crustal magnetic field of Mars using MGS and MAVEN. *J. Geophys. Res. Planets* **124**, 1542–1569 (2019).
- Lillis, R. J., Dufek, J., Bleacher, J. E. & Manga, M. Demagnetization of crust by magmatic intrusion near the Arsia Mons volcano: Magnetic and thermal implications for the development of the Tharsis province, Mars. *J. Volcanol. Geotherm. Res.* **185**, 123–138 (2009).
- Mittelholz, A., Johnson, C. L., Feinberg, J. M., Langlais, B. & Phillips, R. J. Timing of the martian dynamo: new constraints for a core field 4.5 and 3.7 Ga ago. *Sci. Adv.* **6**, eaba0513 (2020).
- Hawke, P. J., Buckingham, A. J. & Dentith, M. C. Modelling source depth and possible origin of magnetic anomalies associated with the Yallalie impact structure, Perth Basin, Western Australia. *Explor. Geophys.* **37**, 191–196 (2006).
- Abramov, O. & Kring, D. A. Numerical modeling of impact-induced hydrothermal activity at the Chicxulub crater. *Meteorit. Planet. Sci.* **42**, 93–112 (2007).
- Melosh, H. J. *Planetary Surface Processes* (Cambridge Univ. Press, 2011).
- Abramov, O. & Kring, D. A. Impact-induced hydrothermal activity on early Mars. *J. Geophys. Res.* **110**, E12S09 (2005).
- Bouley, S. et al. Late Tharsis formation and implications for early Mars. *Nature* **531**, 344–347 (2016).
- Dohm, J. M. & Tanaka, K. L. Geology of the Thaumasia region, Mars: plateau development, valley origins, and magmatic evolution. *Planet. Space Sci.* **47**, 411–431 (1999).
- Flahaut et al. Pristine Noachian crust and key geologic transitions in the lower walls of Valles Marineris: Insights into early igneous processes on Mars. *Icarus* **221**, 420–435 (2012).
- Knapmeyer-Endrun, B. et al. Thickness and structure of the martian crust from InSight seismic data. *Science* **373**, 438–443 (2021).
- Jébrak, M. & Marcoux, E. *Geology of Mineral Resources* (Geological Association of Canada, 2015).
- Bonnemaison, M. & Marcoux, E. Auriferous mineralization in some shear zones: a three-stage model of metallogenesis. *Miner. Depos.* **25**, 96–104 (1990).
- Pirajno, F. & Hoatson, D. M. A review of Australia's Large Igneous Provinces and associated mineral systems: Implications for mantle dynamics through geological time. *Ore Geol. Rev.* **48**, 2–54 (2012).
- Hoatson, D. M. Platinum-group element mineralisation in Australian Precambrian layered mafic-ultramafic intrusions. *AGSO J. Aust. Geol. Geophys.* **17**, 139–151 (1998).
- Phillips, R. J. et al. Ancient geodynamics and global-scale hydrology on Mars. *Science* **291**, 2587–2591 (2001).
- Tsikalas, F. in *Impact Tectonics* (eds Koeberl, K. & Henkel, H.) (Springer, 2005).
- Viviano, C. E., Moersch, J. E. & McSweeney, H. Y. Implications for early hydrothermal environments on Mars through the spectral evidence for



- carbonation and chloritization reactions in the Nili Fossae region. *J. Geophys. Res. Planets* **118**, 1858–1872 (2013).
47. Pascuzzo, A. C., Mustard, J. F., Kremer, C. H. & Ebinger, E. The formation of irregular polygonal ridge networks, Nili Fossae, Mars: implications for extensive subsurface channelized fluid flow in the Noachian. *Icarus* **319**, 852–868 (2019).
  48. Öhman, T., Aittola, M., Kostama, V.-P. & Raitala, J. in *Impact Tectonics* (eds Koeberl, K. & Henkel, H.) (Springer, 2005).
  49. Ojha, L., Karunitillake, S., Karimi, S. & Buffo, J. A magmatic hydrothermal systems on Mars from radiogenic heat. *Nat. Commun.* **12**, 1754 (2021).
  50. Solomon, S. C. et al. New perspectives on ancient Mars. *Science* **407**, 1214–1220 (2005).
  51. Horleston, A. C. et al. The far side of Mars: two distant marsquakes detected by InSight. *TSR* **2**, 88–99 (2022).
  52. Andrews-Hanna, J. C. The formation of Valles Marineris: 1. Tectonic architecture and the relative roles of extension and subsidence. *J. Geophys. Res. Planets* **117**, E03006 (2012).
  53. Platt, J. P. & Vissers, R. L. M. Extensional structures in anisotropic rocks. *J. Struct. Geol.* **2**, 397–410 (1980).
  54. Lister, G. S. & Snoke, A. W. SC mylonites. *J. Struct. Geol.* **6**, 617–638 (1984).
  55. Dennis, A. J. & Secor, D. T. A model for the development of crenulations in shear zones with applications from the Southern Appalachian Piedmont. *J. Struct. Geol.* **9**, 809–817 (1987).
  56. Finch, M. A. et al. The ephemeral development of  $C'$  shear bands: a numerical modelling approach. *J. Struct. Geol.* **139**, 104091 (2020).
  57. Jiang, C., Douté, S., Luo, B. & Zhang, L. Fusion of photogrammetric and photoclinometric information for high-resolution DEMs from Mars in-orbit imagery. *ISPRS J. Photogramm. Remote Sens.* **130**, 418–430 (2017).
  58. Douté, S. & Jiang, C. Small-scale topographical characterization of the Martian surface with in-orbit imagery. *IEEE Trans. Geosci. Remote Sens.* **58**, 447–460 (2020).
  59. Ceamanos, X. et al. Surface reflectance of Mars observed by CRISM/MRO: 1. Multiangle approach for retrieval of surface reflectance from CRISM observations (MARS-ReCO). *J. Geophys. Res. Planets* **118**, 514–533 (2013).
  60. Chouzenoux, E., Legendre, M., Moussaoui, S. & Idier, J. Fast constrained least squares spectral unmixing using primal-dual interior-point optimization. *IEEE J. Sel. Top. Appl. Earth Obs. Remote Sens.* **7**, 59–69 (2014).
  61. Lagarias, J. C., Reeds, J. A., Wright, M. H. & Wright, P. E. Convergence properties of the Nelder-Mead simplex method in low dimensions. *SIAM J. Optim.* **9**, 112–147 (1998).
  62. Fossen, H. *Structural Geology* (Cambridge Univ. Press, 2010).
  63. Schultz, R. A. & Fossen, H. Displacement-length scaling in three dimensions: the importance of aspect ratio and application to deformation bands. *J. Struct. Geol.* **24**, 1389–1411 (2002).
  64. Cowie, P. A. & Scholz, C. H. Physical explanation for the displacement-length relationship of faults using a post-yield fracture mechanics model. *J. Struct. Geol.* **14**, 1133–1118 (1992).
  65. Schultz, R. A. *Geological Fracture Mechanics* (Cambridge Univ. Press, 2019).
  66. Fossen, H. & Cavalcante, G. C. G. Shear zones – A review. *Earth Sci. Rev.* **171**, 434–455 (2017).
  67. MacMillan, R. A. The orientation and sense of displacement of strike-slip faults in continental Crust. Unpubl. thesis, Dept. of Geology, Carleton University, Ottawa, 73 pp. (1975), reproduced in Ranalli, G. Correlation between length and offset in strike-slip faults. *Tectonophysics* **37**, T1–T7 (1977).
  68. Grott, M. & Breuer, D. The evolution of the martian elastic lithosphere and implications for crustal and mantle rheology. *Icarus* **193**, 503–515 (2008).
  69. Mackwell, S. J., Zimmerman, M. E. & Kohlstedt, D. L. High-temperature deformation of dry diabase with application to tectonics on Venus. *J. Geophys. Res. Solid Earth* **103**, 975–984 (1998).
  70. Burov, E. B. & Diament, M. The effective elastic thickness ( $T_e$ ) of continental lithosphere: what does it really mean? *J. Geophys. Res. Solid Earth* **100**, 3905–3927 (1995).
  71. Kohlstedt, D. L., Evans, B. & Mackwell, S. J. Strength of the lithosphere: constraints imposed by laboratory experiments. *J. Geophys. Res. Atmos.* **100**, 17587–17602 (1995).
  72. Grott, M., Hauber, E., Werner, S. C., Kronberg, P. & Neukum, G. High heat flux on ancient Mars: Evidence from rift flank uplift at Coracis Fossae. *Geophys. Res. Lett.* **32**, L21201 (2005).
  73. Ruiz, J., McGovern, P. J. & Tejero, R. The early thermal and magnetic state of the cratered highlands of Mars. *Earth Planet. Sci. Lett.* **241**, 2–10 (2006).
  74. McGovern, P. J. et al. Localized gravity/topography admittance and correlation spectra on Mars: Implications for regional and global evolution. *J. Geophys. Res. Planets* **107**, 5136 (2002).
  75. Karimi, S., Dombard, A. J., Buczkowski, D. L., Robbins, S. J. & Williams, R. M. Using the viscoelastic relaxation of large impact craters to study the thermal history of Mars. *Icarus* **272**, 102–113 (2016).
  76. Solomon, S. C. & Head, J. W. Heterogeneities in the thickness of the elastic lithosphere of Mars: Constraints on heat flow and internal dynamics. *J. Geophys. Res. Solid Earth* **95**, 11073–11083 (1990).
  77. Grott, M., Hauber, E., Werner, S. C., Kronberg, P. & Neukum, G. Mechanical modeling of thrust faults in the Thaumasia region, Mars, and implications for the Noachian heat flux. *Icarus* **186**, 517–526 (2007).
  78. Brugger, J., Wülser, P.-A. & Foden, J. Genesis and preservation of a uranium-rich paleozoic epithermal system with a surface expression (Northern Flinders Ranges, South Australia): radiogenic heat driving regional hydrothermal circulation over geological timescales. *Astrobiology* **11**, 499–508 (2011).
  79. Burov, E. in *Treatise on Geophysics* (ed. Schubert, G.) Ch. 6.03 (Elsevier, 2015).
  80. Mohit, P. S. & Phillips, R. J. Viscous relaxation on early Mars: a study of ancient impact basins. *Geophys. Res. Lett.* **34**, L21204 (2007).
  81. Karato, S.-I., Paterson, M. S. & FitzGerald, J. D. Rheology of synthetic olivine aggregates: Influence of grain size and water. *J. Geophys. Res. Solid Earth* **91**, 8151–8176 (1986).
  82. Shelton, G. & Tullis, J. Experimental flow laws for crustal rocks. *Eos Trans. AGU* **62**, 396 (1981).
  83. Caristan, Y. The transition from high temperature creep to fracture in Maryland diabase. *J. Geophys. Res. Solid Earth* **87**, 6781–6790 (1982).
  84. Poort, J. & Klerkx, J. Absence of a regional surface thermal high in the Baikal rift; new insights from detailed contouring of heat flow anomalies. *Tectonophysics* **383**, 217–241 (2004).
  85. Craddock, R. A. & Maxwell, T. A. Geomorphic evolution of the Martian highlands through ancient fluvial processes. *J. Geophys. Res. Planets* **98**, 3453–3468 (1993).
  86. Grott, M., Morschhauser, A., Breuer, D. & Hauber, E. Volcanic outgassing of CO<sub>2</sub> and H<sub>2</sub>O on Mars. *Earth Planet. Sci. Lett.* **308**, 391–400 (2011).
  87. Quesnel, Y. et al. Serpentinization of the martian crust during Noachian. *Earth Planet. Sci. Lett.* **277**, 184–193 (2009).
  88. Yamato, P. et al. Burial and exhumation in a subduction wedge: mutual constraints from thermomechanical modeling and natural P-T-t data (Schistes Lustrés, western Alps). *J. Geophys. Res. Solid Earth* **112**, B07410 (2007).
  89. Polonia, A. et al. Lower plate serpentinite diapirism in the Calabrian Arc subduction complex. *Nat. Commun.* **8**, 2172 (2017).
  90. Langlais, B., Purucker, M. E. & Manda, M. Crustal magnetic field of Mars. *J. Geophys. Res. Planets* **109**, E02008 (2004).
  91. Malin, M. C. et al. Context camera investigation on board the mars reconnaissance orbiter. *J. Geophys. Res. Planets* **112**, E05S04 (2007).
  92. Christensen, P. R., Gorelick, N. S., Mehall, G. L. & Murray, K. C. THEMIS public data releases, planetary data system node, Arizona State University. <http://themis-data.asu.edu> (2006).
  93. Smith, D., Zuber, M. T., Neumann, G. A. & Jester, P. Mars global surveyor laser altimeter precision experiment data record, NASA Planetary Data System, MGS-M-MOLA-3-PEDR-L1A-V1.0 (2003).

## Acknowledgements

This work was funded by OPUS/V-MACS project no. 2015/17/B/ST10/03426 of the National Science Center, Poland, and the EXOMHYDR project. The EXOMHYDR project is carried out within the TEAM program of the Foundation for Polish Science, co-financed by the European Union under the European Regional Development Fund. F.S. and B.L. acknowledge support from the Institut National des Sciences de l'Univers (INSU), the Centre National de la Recherche Scientifique (CNRS), and the Centre National d'Etudes Spatiales (CNES) through the Program National de Planétologie. S.D. is grateful to the Centre National d'Etudes Spatiales (CNES) for supporting his CaSSIS and HiRISE related work through the Program “Exobiologie, protection planétaire et exoplanètes”.

The authors are indebted to Richard A. Schultz (Orion Geomechanics LLC) for the suggestion to investigate the relationships between the shear zones in Valles Marineris and the Borealis basin, and for insightful discussions.

## Author contributions

J.G. designed and coordinated the study, conducted the mineralogical analysis, contributed to the structural analysis, and wrote most of the manuscript. D.M. obtained the funding for this work, conducted the structural and geophysical analysis, contributed to the mineralogical analysis, and to manuscript writing. F.S. developed the spectral unmixing method and ran the code, and wrote the corresponding method. S.D. generated the HiRISE digital elevation model and wrote the corresponding method. B.L. provided the magnetic dataset, guided its interpretation, and contributed to manuscript writing.

## Competing interests

The authors declare no competing interests.

**Additional information**

**Supplementary information** The online version contains supplementary material available at <https://doi.org/10.1038/s43247-022-00612-5>.

**Correspondence** and requests for materials should be addressed to Joanna Gurgurewicz.

**Peer review information** *Communications Earth & Environment* thanks Chris Okubo, Bob Myhill and the other, anonymous, reviewer(s) for their contribution to the peer review of this work. Primary Handling Editors: Claire Nichols, Joe Aslin. Peer reviewer reports are available.

**Reprints and permission information** is available at <http://www.nature.com/reprints>

**Publisher's note** Springer Nature remains neutral with regard to jurisdictional claims in published maps and institutional affiliations.



**Open Access** This article is licensed under a Creative Commons Attribution 4.0 International License, which permits use, sharing, adaptation, distribution and reproduction in any medium or format, as long as you give appropriate credit to the original author(s) and the source, provide a link to the Creative Commons license, and indicate if changes were made. The images or other third party material in this article are included in the article's Creative Commons license, unless indicated otherwise in a credit line to the material. If material is not included in the article's Creative Commons license and your intended use is not permitted by statutory regulation or exceeds the permitted use, you will need to obtain permission directly from the copyright holder. To view a copy of this license, visit <http://creativecommons.org/licenses/by/4.0/>.

© The Author(s) 2022